Delft University of Technology

A numerical benchmark for modelling phase change in molten salt reactors

Pater, Mateusz; Kaaks, Bouke; Lauritzen, Bent; Lathouwers, Danny

DOI
10.1016/j.anucene.2023.110093

Publication date
2023

Document Version
Final published version

Published in
Annals of Nuclear Energy

Citation (APA)
Pater, M., Kaaks, B., Lauritzen, B., & Lathouwers, D. (2023). A numerical benchmark for modelling phase change in molten salt reactors. *Annals of Nuclear Energy*, *194*, Article 110093. https://doi.org/10.1016/j.anucene.2023.110093

Important note
To cite this publication, please use the final published version (if applicable).
Please check the document version above.

Copyright
Other than for strictly personal use, it is not permitted to download, forward or distribute the text or part of it, without the consent of the author(s) and/or copyright holder(s), unless the work is under an open content license such as Creative Commons.

Takedown policy
Please contact us and provide details if you believe this document breaches copyrights.
We will remove access to the work immediately and investigate your claim.

This work is downloaded from Delft University of Technology.
For technical reasons the number of authors shown on this cover page is limited to a maximum of 10.

Annals of Nuclear Energy 194 (2023) 110093

Contents lists available at ScienceDirect

Annals of Nuclear Energy

journal homepage: www.elsevier.com/locate/anucene

A numerical benchmark for modelling phase change in molten salt reactors

Mateusz Pater [a,c,1], Bouke Kaaks [b,*,1], Bent Lauritzen [a], Danny Lathouwers [b]

[a] Technical University of Denmark, Department of Physics, Frederiksborgvej 399, 4000 Roskilde, Denmark
[b] Delft University of Technology, Department of Radiation Science and Technology, Mekelweg 15, 2629 JB Delft, The Netherlands
[c] Seaborg Technologies, Titangade 11, 2200 Copenhagen N, Denmark

ARTICLE INFO

Dataset link: https://doi.org/10.5281/zenodo.7821693

Keywords:
Phase change
Melting
Molten salt reactor
Benchmark
Freeze valve

ABSTRACT

The design of a molten salt reactor is largely based on CFD simulations. Phase change plays an important role in the safety of the reactor, but numerical modelling of phase change is particularly challenging. Therefore, the knowledge of the margin of error of CFD simulations involving phase change is very important. Relevant experimental validation data is lacking. For this reason, a numerical benchmark designed after the freeze valve is proposed. The benchmark consists of five stages, where with each step more complexity is added. The stepwise addition of complexity allows for pinpointing potential sources of discrepancy. Results were obtained with three different codes: STAR-CCM+, OpenFOAM, and DGFlows. The results were found to be largely consistent between the codes, however the addition of conjugate heat transfer introduced some discrepancies. These results indicate that careful consideration is needed when coupling conjugate heat transfer solvers with solid–liquid phase change models.

1. Introduction

Solid–liquid phase change plays an important role in many applications, such as latent heat storage (see Faden et al., 2019b), metallurgy (see Ben-David et al., 2013), and the design of the Molten Salt Fast Reactor (MSFR) (see Cartland Glover et al., 2019, Tiberga et al., 2020a, and Voulgaropoulos et al., 2020). Due to the mathematical complexity of solid–liquid phase change as a moving boundary problem, extensive research has been conducted on its analytical and numerical solution since the end of the 19th century. Stefan (1889) formulated a simple one-dimensional melting problem, to which an analytical solution can be found. Subsequent efforts were devoted to solving Stefan problems in multiple dimensions (see Friedman, 1968 and Wilson et al., 1978), coupled with fluid flow (e.g. by Dantzig, 1989 and Voller and Swaminathan, 1991), and using different properties for the solid and the liquid phases (see for instance Belhamadia et al., 2012). Most phase change problems of industrial relevance require numerical solutions, and recent advancements in computing power allowed an increase in the accuracy and complexity of the different models.

The present work was performed in the context of the development of the MSFR under the framework of the SAMOFAR (2014) and SAMOSAFER (2018) projects. A key and unique safety component of the MSFR is the freeze valve, which is designed to melt in case of an accident scenario (see for instance Chisholm et al., 2020 for a recent and comprehensive overview of the freeze valve design and development). A sufficiently short opening time of the valve is required to drain the reactor quick enough to prevent the temperature from exceeding dangerously high values, as stated by Tiberga et al. (2020a). Apart from experimental investigations such as those performed by Giraud et al. (2019), the design of the freeze valve relies heavily on numerical simulations to obtain predictions of its melting time. Experimental studies suitable for numerical validation have mainly focused on the melting of pure metals or paraffin wax in rectangular or cylindrical enclosures, such as those performed by Gau and Viskanta (1986), Jones et al. (2006), and Faden et al. (2019a) and do not include the full complexity of the MSFR freeze valve design. For this reason, it is of paramount importance that sufficient knowledge is obtained regarding the accuracy of currently used numerical modelling approaches and their possible limitations in predicting the melting behaviour of the MSFR and any other similar freeze valve design.

Recently, a multiphysics numerical benchmark for codes dedicated to the MSFR was proposed (Tiberga et al., 2020c), and results were compared for six different codes (Tiberga et al., 2020b, Blanco et al., 2020, Cervi et al., 2019, Fiorina et al., 2015, Groth-Jensen et al., 2021). The simplicity of the benchmark and its step-by-step approach made it a suitable tool for testing the performance of various codes and detecting possible discrepancies. In a similar fashion, we propose a two-dimensional numerical benchmark based on one of the MSFR

* Corresponding author.
E-mail address: B.J.Kaaks@tudelft.nl (B. Kaaks).
[1] Both are first authors.

https://doi.org/10.1016/j.anucene.2023.110093
Received 13 April 2023; Received in revised form 7 July 2023; Accepted 15 August 2023
Available online 25 August 2023
0306-4549/© 2023 The Author(s). Published by Elsevier Ltd. This is an open access article under the CC BY license (http://creativecommons.org/licenses/by/4.0/).

freeze valve designs (Giraud et al., 2019), to compare the solid–liquid phase change modelling capabilities and their coupling with fluid flow and conjugate heat transfer models of different numerical codes. The benchmark consists of five different stages and with each stage, complexity is added as the model evolves towards a more realistic representation of the MSFR freeze valve. The first stage consists of a variation on the classical Stefan problem, however featuring a time-dependent temperature boundary condition that is representative of shut-down conditions in the MSFR. In the second stage, volumetric heating is added to model the influence of radiation and heat deposition from the fuel salt on the melting of the freeze plug. In the third stage, solid walls are added to the freeze valve geometry and conjugate heat transfer modelling is required in addition to solving the melting problem. In the fourth stage, the role of natural convection on the melting behaviour is investigated, and in the fifth and final stage, forced convection is added, mimicking the recirculation of the fuel salt above the freeze valve. In this work, three different numerical codes are used to compare the results for the five benchmark stages: an in-house code DGFlows developed at Delft University of Technology (Hennink et al., 2021, Tiberga et al., 2020a, Kaaks et al., 2023), the commercial code STAR-CCM+ (Siemens Digital Industries Software), and the open-source code OpenFOAM (Weller et al., 1998). The step-wise addition of complexity allowed for identifying at which steps discrepancies between the results provided by the codes would arise.

The remainder of this work is organized as follows. In Section 2, a brief introduction is given to the numerical challenge of solving solid–liquid phase change problems. Subsequently, in Section 3, the various modelling approaches of the three codes are presented. In Section 4, the five benchmark stages are introduced, and the results of the codes are discussed and compared. Finally, Section 5 summarizes the most important results of this MSFR freeze valve numerical benchmark study and presents the conclusions.

2. Challenge of modelling solid–liquid phase change

Standard notation is used throughout the document unless otherwise specified. The enthalpy transport equation in conservative form is written as:

$$\frac{\partial H}{\partial t} + \nabla \cdot (\boldsymbol{u} H) = \nabla \cdot (\lambda \nabla T), \tag{1}$$

where H is enthalpy, t is time, $\boldsymbol{u}$ is velocity, λ is heat conductivity, and T is temperature. For most heat transfer problems, the enthalpy-temperature relationship is smooth and the temperature gradient in the diffusion term may be expressed in terms of the enthalpy ($\nabla T = \frac{1}{\rho c_p} \nabla H$, with ρ being density and c_p heat capacity), hereby eliminating the temperature as the unknown and resulting in a linear energy transport equation that can be solved with standard solution methods. In contrast, solid–liquid phase change is characterized by a jump in enthalpy at the melting point, leading to a non-smooth enthalpy-temperature relationship (see Fig. 1).

Assuming constant thermophysical properties in each phase, the temperature-enthalpy relationship reads:

$$T(H) = \begin{cases} \dfrac{H}{\rho_s c_{p,s}}, & H \le \rho_s c_{p,s} T_m \\ T_m, & \rho_s c_{p,s} T_m < H < \rho_s c_{p,s} T_m + \rho_l L \\ T_m + \dfrac{H - (\rho_s c_{p,s} T_m + \rho_l L)}{\rho_l c_{p,l}}, & H \ge \rho_s c_{p,s} T_m + \rho_l L \end{cases} \tag{2}$$

where ρ_s is the density of the solid and ρ_l of the liquid phase, $c_{p,s}$ is the heat capacity of the solid and $c_{p,l}$ of the liquid phase, T_m is the melting point, and L is the latent heat of the solid–liquid phase change. With this temperature-enthalpy relationship, the energy equation becomes highly non-linear. Therefore, the challenge in modelling solid–liquid phase change problems is to solve the energy equation with the non-smooth enthalpy-temperature coupling and to accurately track the displacement of the solid–liquid interface.

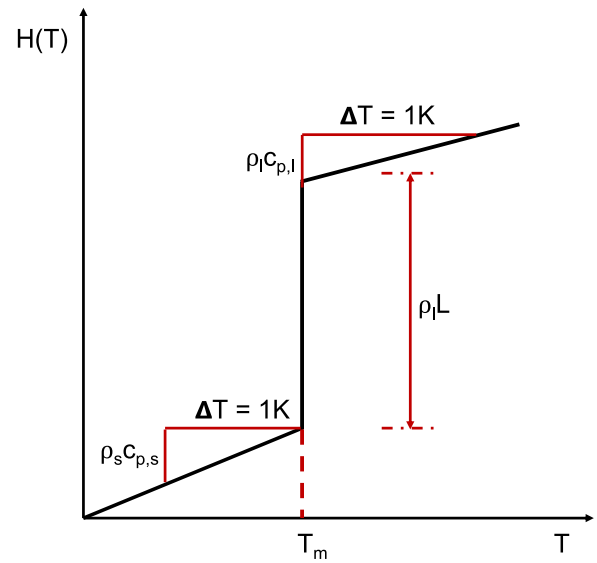

Fig. 1. Enthalpy-temperature relationship for an isothermal solid–liquid phase change. The slope of the solid region depends on the density ρ_s and heat capacity $c_{p,s}$ of the solid phase, whereas the slope of the liquid region depends on the density ρ_l and heat capacity $c_{p,l}$ of the liquid phase. The magnitude of the enthalpy jump depends on the liquid density and the latent heat L.

Numerical methods for solving solid–liquid phase change problems are characterized by certain limitations which we describe below. First of all, the discontinuous enthalpy and material properties at the solid–liquid interface may lead to strong gradients which are difficult to resolve numerically. Therefore, many phase change models assume that properties such as density or thermal conductivity remain temperature-independent and utilize an approximation function such that the enthalpy change is modelled smoothly over a predefined temperature range (the so-called mushy zone). In addition, a very fine mesh is often needed in the vicinity of the solid–liquid interface to accurately resolve the gradients. In particular the density change, and accompanying volume changes and secondary flow effects, can be challenging from a numerical modelling perspective. Accurate modelling of the density change during solid–liquid phase change would require the use of a fully compressible fluid approach and special treatment of the volume expansion effects, as shown by Faden et al. (2021). To reduce complexity of the numerical approach and not distract from the focus of the benchmark, we assumed a constant density in our simulations.

Furthermore, modelling the flow within the (porous) solid–liquid interface zone may be a considerable challenge. In our case, we considered isothermal phase change and we did not consider microscale phase change phenomena (such as phase segregation, dendrite formation etc. analysed by Tano et al., 2017). Therefore, we have a sharp interface between the solid and the liquid salt, and the Navier–Stokes equations may be solved by simply damping the velocities in the solid phase. Lastly, strong temperature gradients at the interface and accompanying thermal stresses may produce cracking phenomena in the solid. Modelling these phenomena requires the coupling of the phase change model to an additional solid mechanics model and was not considered in the present work.

3. Characteristics of the codes used

A short description of each code used in this benchmark is presented below.

3.1. STAR-CCM+

The following description of STAR-CCM+ version 2020.2 used in this benchmark is based on the User Guide (Siemens Digital Industries Software). CFD modules of STAR-CCM+ utilize the finite volume method and solve the Navier–Stokes equations in each computational cell. The software is able to model multiphase flow using Eulerian and Lagrangian approaches.

3.1.1. Volume of fluid

A phase change problem is a multiphase problem, as more than one thermodynamic state of the matter – in our case, solid and liquid – are present and interact with each other within the same system. In order to model phase change in STAR-CCM+, the Volume of Fluid approach, traditionally used for tracking interfaces between gases and liquids (Hirt and Nichols, 1981), is used by the software. Volume of Fluid is a simple model based on the Eulerian formulation of a multiphase fluid, where two or more immiscible phases share an interface. Mass, momentum, and energy are treated as mixture quantities rather than phase quantities. The dynamic viscosity and thermal conductivity are volume-weighted, and the specific heat is mass-weighted. Conservation equations are solved for the mixture in a computational cell. The mesh must be fine enough to resolve the interface between the phases.

Phases are described by the phase volume fraction α_i:

$$\alpha_i = \frac{V_i}{V}, \tag{3}$$

where V_i is the volume of phase i in the cell of volume V. The phase mass conservation equation is:

$$\frac{\partial}{\partial t}\int_V \alpha_i \, dV + \oint_A \alpha_i \boldsymbol{v} \cdot d\boldsymbol{A} = \int_V \left(S_{\alpha_i} - \frac{\alpha_i}{\rho_i}\frac{D\rho_i}{Dt} \right) dV - \int_V \frac{1}{\rho_i} \nabla \cdot (\alpha_i \rho_i \boldsymbol{v}_{d,i}) \, dV, \tag{4}$$

where $\boldsymbol{A}$ is the surface area vector, $\boldsymbol{v}$ is the mixture velocity, $\boldsymbol{v}_{d,i}$ is the diffusion velocity, S_{α_i} is a source term of phase i, and $D\rho_i/Dt$ is the Lagrangian derivative of the phase densities ρ_i.

A Segregated Multiphase Temperature model is activated in STAR-CCM+ in order to solve the total energy equation. The temperature is the solved variable and the enthalpy is computed from the temperature according to the multiphase equation of state. In our STAR-CCM+ model, the convective flux in the Volume of Fluid transport equation is discretized using a second-order scheme. The second-order convection scheme is used to solve the energy equation as well.

3.1.2. Melting-solidification

The solid–liquid interface is not tracked directly by the software; instead, an enthalpy formulation is used to determine the relative fraction of the solid and liquid phases:

$$H^*_{ls} = H_{ls} + (1 - \alpha^*_s)L, \tag{5}$$

where H^*_{ls} is the enthalpy of the liquid–solid phase, H_{ls} is the sensible enthalpy, L is the latent heat and α^*_s is the relative solid volume fraction. For linearized melting, the liquid fraction corresponds to the fraction of the latent heat of fusion that has been absorbed by the system. In STAR-CCM+, each mesh cell is characterized by an individual value of the relative solid volume fraction. If the material's solidus and liquidus points are the same, a difference of 0.002 K is introduced automatically between them so that it is possible for the software to take the latent heat into account in a phase change problem. This way, the relative solid volume fraction between fully solid and fully liquid states is calculated as:

$$\alpha^*_s = \frac{T_{liquidus} - T}{T_{liquidus} - T_{solidus}}. \tag{6}$$

One of the optional models for phase change in STAR-CCM+ is a Melting-Solidification Flow Stop model. With the help of this functionality, the flow is stopped in a cell when a specified solid fraction is exceeded. To avoid assigning velocities to the cells undergoing melting and to resemble the way in which DGFlows and OpenFOAM treat phase change, the default solid fraction value of 1 has been changed to 0.01. This way, the momentum equations are solved only in the cells that have (almost) fully undergone phase change to the liquid state.

3.1.3. Conjugate heat transfer

Coupled heat transfer between a liquid and an adjoining solid, i.e. conjugate heat transfer, is modelled with the use of an interface between the two materials. Each material has its own thermal boundary conditions, and the interface can have an additional heat source S. The energy conservation equation at the interface is:

$$q_{fluid} + q_{solid} = -S, \tag{7}$$

where q_{fluid} is the normal heat flux value from the fluid through the boundary and q_{solid} is the normal heat flux value leaving through the boundary into the solid. The equation is solved for each side of the interface with the use of a linearized heat flux taking into account secondary gradients:

$$\boldsymbol{q} = \lambda \left[(T_w - T_c)\boldsymbol{B} + \nabla T_c - (\nabla T_c \cdot \boldsymbol{\Delta x})\boldsymbol{B} \right] \tag{8a}$$

$$\boldsymbol{B} = \frac{\hat{\boldsymbol{n}}}{\boldsymbol{n} \cdot \hat{\Delta x}} \tag{8b}$$

$$\boldsymbol{\Delta x} = \boldsymbol{x_1} - \boldsymbol{x_0}, \tag{8c}$$

where T_w and T_c are the wall and cell temperatures, respectively, $\hat{\boldsymbol{n}}$ is the normal vector, and $\boldsymbol{\Delta x}$ is a vector pointing from the centroid of cell 0 to the centroid of cell 1, lying on opposing sides of the interface.

3.2. OpenFOAM

OpenFOAM (Weller et al., 1998) is the leading open-source CFD software. In this work, a phase-change model based on the 'linearized enthalpy approach' (Kaaks et al., 2022, Kaaks et al., 2023) has been implemented in OpenFOAM v8, distributed by the OpenFOAM foundation. The 'linearized enthalpy approach' is based on the conservative form of the enthalpy transport equation (see Eq. (1)) and builds on the work of Faden et al. (2019a), Nedjar (2002), and Swaminathan and Voller (1993). Using the 'linearized enthalpy approach', the volumetric enthalpy is linearized around the latest known temperature value:

$$H^{n+1,i+1} = H^{n+1,i} + \frac{dH}{dT}\left(T^{n+1,i+1/2} - T^{n+1,i}\right), \tag{9}$$

where $n+1$ refers to the latest time-step, $i+1$ refers to the newest iteration, i indicates the previous iteration, and $i + 1/2$ denotes the use of an intermediate value. Here, the following approximation for the enthalpy-temperature derivative is used:

$$\frac{dH}{dT} \approx \frac{1}{2}\left(\rho_s c_{p,s} + \rho_l c_{p,l}\right). \tag{10}$$

Performing the second order accurate BDF2 time integration and replacing the unknown enthalpy with the linearized enthalpy yields the 'linearized enthalpy equation':

$$\frac{dH}{dT}\left(\frac{3T^{n+1,i+1/2}}{2\Delta t} + \nabla \cdot \left(\boldsymbol{u}T^{n+1,i+1/2}\right)\right) - \nabla \cdot \left(\lambda \nabla T^{n+1,i+1/2}\right) = \frac{dH}{dT}\left(\frac{3T^{n+1,i}}{2\Delta t}\right) - \frac{3H^{n+1,i} - 4H^n + H^{n-1}}{2\Delta t}. \tag{11}$$

Here we use the 'sensible enthalpy only' formulation for the heat convection term (König-Haagen et al., 2020).

The 'linearized enthalpy equation' is linear in the unknown temperature and is iterated until convergence. At each iteration, the volumetric enthalpy at the cell centres is updated and the temperature is recalculated according to the enthalpy-temperature relationship (see Eq. (2)):

$$H^{n+1,i+1} = H^{n+1,i} + \frac{dH}{dT}\left(T^{n+1,i+1/2} - T^{n+1,i}\right) \tag{12a}$$

$$T^{n+1,i+1} = T(H^{n+1,i+1}). \tag{12b}$$

The non-linear enthalpy-temperature iterations are terminated when the following convergence criterion is reached:

$$max\left[res, \sum_{n_{elem}=0}^{n_{elem}=N_{elem}} \left(T^{n+1,i+1} - T^{n+1,i}\right)\right] < tol. \tag{13}$$

In this work, $tol = 10^{-6}$. Here, res is the initial residual of the iterative matrix solver and N is the total number of cells. Upon convergence, the difference between the old and the new temperature values approaches zero and the solution to the 'linearized enthalpy equation' approaches the solution to the original enthalpy transport equation in conservative form.

A no-slip condition at the solid–liquid interface is enforced using the 'Darcy source term' approach (Brent et al., 1988, König-Haagen et al., 2017) and natural convection is treated through the Boussinesq approximation. As such, the momentum equation reads:

$$\frac{\partial\left(\rho_l \boldsymbol{u}\right)}{\partial t} + \nabla\cdot\left(\boldsymbol{u}\otimes\left(\rho_l\boldsymbol{u}\right)\right) = \nabla\cdot\left[\mu\left(\nabla\boldsymbol{u} + (\nabla\boldsymbol{u})^T\right)\right] - \nabla p + \rho_l \boldsymbol{g}\beta(T - T_m) - C\frac{(1-\alpha)^2}{\alpha^3 + b}\boldsymbol{u}. \tag{14}$$

Here, C is a large parameter (10^{10} in this work) and b is a small parameter to avoid division by zero (10^{-3} in this work); μ is the dynamic viscosity, p is the pressure, $\boldsymbol{g}$ is the gravitational acceleration, and β is the thermal expansion coefficient.

To model the conjugate heat transfer, the total mesh is separated into a metal and a salt part. Separate matrix equations are solved for each part, and the temperature at the interface between the metal and the salt is calculated through harmonic averaging:

$$T_{IF,metal} = \frac{T_{nearest,metal}\times\left(\lambda_{metal}/\delta_{metal}\right) + T_{nearest,salt}\times\left(\lambda_{salt}/\delta_{salt}\right)}{\lambda_{metal}/\delta_{metal} + \lambda_{salt}/\delta_{salt}} \tag{15}$$

Here, $T_{nearest}$ is the temperature at the nearest cell-centre of the metal and salt domain respectively, and δ is the distance from the cell centre to the interface.

The full solution algorithm is as follows:

1. Solve the momentum equation in the salt part.
2. Solve the energy equation in the salt part through a series of non-linear enthalpy-temperature iterations.
3. Perform the pressure correction in the salt part (in this work, 3 corrector steps are used).
4. Solve the energy equation in the metal part.
5. Repeat steps 1–4 until the total number of outer iterations has been reached.

3.3. DGFlows

DGFlows is an in-house CFD code based on the discontinuous Galerkin Finite Element Method (DG-FEM), developed at the Radiation Science and Technology Department of Delft University of Technology (Hennink et al., 2021, Tiberga et al., 2020a). DG-FEM combines attractive features of the finite element and finite volume methods, such as an arbitrarily high order of accuracy, high geometric flexibility, local conservation of vector and scalar fields, possibility for upwinding and a compact numerical stencil facilitating efficient parallelization of the solution procedure (Tiberga et al., 2020a, Hennink et al., 2021). To model phase change, the 'linearized enthalpy approach' has been implemented in DGFlows. The DG-FEM variational formulation of the coupled system of energy, momentum, and non-linear enthalpy-temperature coupling equations reads (Kaaks et al., 2023):

$$Find \quad m_h \in \mathcal{V}^d_{h,m} \quad and \quad p_h \in \mathcal{V}_{h,p,H,T} \quad and \quad H_h \in \mathcal{V}_{h,p,H,T} \quad and \quad T_h \in \mathcal{V}_{h,p,H,T}$$
$$such \quad that \quad \forall v_h \in \mathcal{V}^d_{h,m} \quad and \quad \forall q_h, \forall w_h \in \mathcal{V}_{h,p,H,T},$$

$$\sum_{\mathcal{T}\in\mathcal{T}_h}\int_{\mathcal{T}} \boldsymbol{v}_h\cdot\frac{\partial \boldsymbol{m}_h}{\partial t} + a^{conv}(\boldsymbol{u}_h, \boldsymbol{m}_h, \boldsymbol{v}_h) + a^{diff}(\boldsymbol{m}_h, \boldsymbol{v}_h) + a^{div}(\boldsymbol{v}_h, p_h) + a^{source}(\boldsymbol{m}_h, \boldsymbol{v}_h) = l^{conv}(\boldsymbol{u}_h, \boldsymbol{m}_h\mathbf{v}_h) + l^{diff}(\boldsymbol{v}_h) + l^{source}(\boldsymbol{v}_h, T_h) \tag{16a}$$

$$a^{div}(\boldsymbol{m}_h, q_h) = l^{div}(q_h) \tag{16b}$$

$$\sum_{\mathcal{T}\in\mathcal{T}_h}\int_{\mathcal{T}} w_h\frac{\partial H_h}{\partial t} + a^{conv}(\boldsymbol{m}_h, T_h, w_h) + a^{diff}(T_h, w_h) = l^{conv}(\boldsymbol{u}_h, w_h) + l^{diff}(w_h) \tag{16c}$$

$$T_h = T(H_h). \tag{16d}$$

Here, $\mathbf{m}$ is the mass flux, $\mathbf{u}$ is the velocity, H is the enthalpy, T is the temperature and p is the pressure. a and l correspond to the bilinear and the linear forms respectively, with the superscripts '$conv$', '$diff$', 'div', and '$source$' referring to the contributions from the convection, diffusion, divergence and source terms respectively. Finally, $\mathcal{T}$ defines the local element and the subscript 'h' defines the finite element approximation. A hierarchical set of orthogonal basis and test functions (normalized Legendre polynomials) are used to approximate each variable within the elements. Here, the test functions are represented by the letters 'v', 'w' and 'q' and the function space is denoted by $\mathcal{V}$. A mixed order formulation is used, that is $\mathcal{P}_{p,H,T} = \mathcal{P}_m - 1$, where '$\mathcal{P}$' is the polynomial order of the finite element approximation. The symmetric interior penalty (SIP) method is used to discretize the diffusion term, and the Lax–Friedrichs numerical flux is used to discretize the convection terms.

The non-linear enthalpy-temperature iterations are performed in a similar manner as the implementation of the 'linearized enthalpy approach' in OpenFOAM. For more detailed information on the implementation and validation of the DG-FEM formulation of the 'linearized enthalpy approach', please refer to Kaaks et al. (2023). To model the conjugate heat transfer, a material identifier is used to distinguish the metal and the salt parts of the domain. The momentum equation is only solved within the salt, where the no-slip boundary condition is applied at the metal-salt interface. The enthalpy transport equation is solved for the full domain. Here, continuity at the solid–liquid interface is already imposed through the penalty terms in the SIP discretization of the heat diffusion, and therefore no additional treatment is required.

Time-stepping is performed using the second order BDF2 method. All integrals are evaluated through Gaussian quadrature with a polynomial accuracy of $3P_m - 1$. Meshes are generated with the open-source software tool Gmsh by Geuzaine and Remacle (2009) and METIS by Karypis and Kumar (1998) is used to partition the mesh. The resulting matrix equations are solved with iterative Krylov methods using the PETSc library (Balay et al., 1997).

4. Results and discussion of the numerical benchmark study

A numerical benchmark is proposed based on the MSFR freeze valve design described by Giraud et al. (2019). The freeze valve is a key passive safety feature unique to the MSFR, and is designed to melt in the case of a reactor anomaly, draining the fuel salt into an emergency drainage system. The goal of the benchmark study is to provide a first indication of the consistency between different solid–liquid phase-change modelling approaches, and to identify possible sources of discrepancies between the codes. The benchmark consists of five stages, where with each new stage an additional level of complexity is introduced, as the model converges towards a more realistic design of the MSFR freeze valve. At each stage, the calculated temperatures, position of the melting front, and velocities are compared amongst the three different codes.

In the first stage of the benchmark, the fuel salt undergoes melting inside a two-dimensional cavity encompassing the salt domain. The heat source, modelled after the decay heat of the MSFR, is located at the top boundary of the model. The heat is conducted towards the bottom part of the domain, where phase change takes place. In

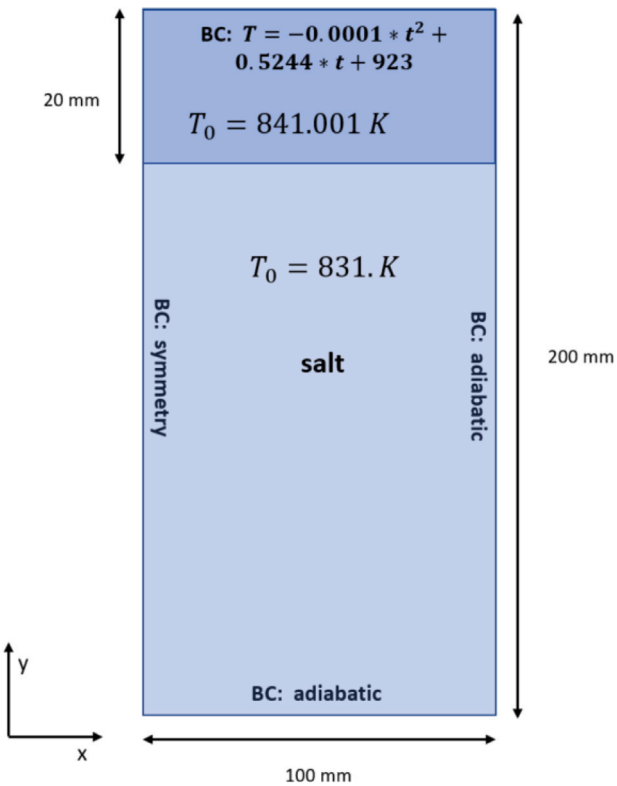

Fig. 2. Geometry with boundary (marked as "BC") and initial conditions (marked as T_0) of stage 1. The dark blue colour indicates the molten salt, and the light blue colour indicates the solid salt.

the second stage, a volumetric heat source is added to the entire salt volume to mimic the heat deposition due to neutrons and photons arriving at the freeze valve's location, originating from the reactor core above. This heat source follows a similar time-dependent function as the decay heat. In the third stage, a solid wall is added to the side of the freeze valve geometry. Conjugate heat transfer is modelled to investigate the effect of heat conduction in the metal and subsequent heat exchange between the salt domain and the metal wall resulting in the melting of salt next to the wall. In the fourth stage, momentum equations are implemented with the use of a Boussinesq approximation, and the natural circulation takes place in the salt volume, making the melting process more realistic. In the last, fifth stage of the benchmark, movement of the top boundary is added to impose forced convection that is present in the reactor, where the molten fuel salt above the freeze valve is recirculated.

4.1. Stage 1

4.1.1. Description

To accommodate as many different software suites as possible and to keep the computational cost affordable, a two-dimensional Cartesian geometry was chosen for the benchmark. Due to the symmetric nature of the modelled freeze valve, the geometry is cut in half at the symmetry axis to save computational resources.

The model geometry is a 200 mm high and 100 mm wide rectangle (see Fig. 2). The bottom and right boundaries are adiabatic, no-slip walls. The left boundary is the symmetry axis. The symmetry axis is characterized by the normal components and gradients of all variables being set to zero, and zero fluxes across the axis. The top boundary is a no-slip wall with a variable-temperature boundary condition.

The decay heat of the MSFR expressed as power P is characterized by the following formula derived by Tano Retamales et al. (2018):

$$P(t) = 6.45908 \cdot 10^6 - 6.92 \cdot 10^5 \cdot \ln(t) \qquad (\mathrm{W\,m^{-3}}), \tag{17}$$

Table 1
Thermophysical properties of the salt used in the benchmark.

Property	Value	Unit
T_m	841	K
L	159	$\mathrm{kJ\,kg^{-1}}$
$\rho_s = \rho_l$	4390	$\mathrm{kg\,m^{-3}}$
$\lambda_s = \lambda_l$	1.5	$\mathrm{W\,m^{-1}\,K^{-1}}$
$c_{p,s}$	815	$\mathrm{J\,kg^{-1}\,K^{-1}}$
$c_{p,l}$	1000	$\mathrm{J\,kg^{-1}\,K^{-1}}$
β	$2.5 \cdot 10^{-4}$	$\mathrm{K^{-1}}$
μ	$7.5 \cdot 10^{-3}$	Pa s

with t measured in seconds. From the decay heat, Tiberga et al. (2019) derived an equation for the average temperature of the shut-down reactor:

$$T(t) = -0.0001t^2 + 0.5244t + 923 \qquad (\mathrm{K}), \tag{18}$$

which is used as the time-dependent boundary condition at the upper wall that controls the melting process. The bottom 90% of the freeze valve geometry is initially at 831 K (frozen salt), i.e. there is 10 K of subcooling, and the top 10% is just above the melting point, at 841.001 K.

Since the essence of the benchmark is the phase change modelling and associated fluid flow and conjugate heat transfer, we use the same constant density for the solid and for the liquid phase. The thermophysical properties of the salt, taken from Tiberga et al. (2019), are listed in Table 1.

The computational grid is uniform and made up from 200 × 100 squares. The time step is 0.5 s. A set of different time steps and mesh refinements were investigated in a sensitivity analysis. The time steps analysed on the 200 × 100 mesh were the following: 2.0, 1.0, 0.5, and 0.1 s. The mesh refinements with the 0.5 s time step were: 50 × 25, 100 × 50, 200 × 100, and 400 × 200. Stage 1 is in principle a one-dimensional heat conduction problem. Temperatures and the melting front at the centreline after 2500 s obtained by the three codes are directly compared.

4.1.2. Implementation

In both OpenFOAM and STAR-CCM+, the diffusion terms were discretized using a central differencing scheme and a second order upwind scheme was used for the convection terms. Therefore, both the velocity and the temperature are second order accurate in space. In DGFlows, linear elements were used for the temperature, enthalpy, and pressure, and quadratic elements were used for the velocity (recall the use of a mixed order formulation), leading to a second order accurate discretization of the temperature, enthalpy, and pressure, and a third order accurate discretization of the velocity. In all three codes, a second order implicit time-stepping scheme was used (i.e. BDF2).

In STAR-CCM+, in stages 1–3, a maximum number of 30 inner iterations were used as a stopping criterion for the implicit unsteady solver. The segregated flow solver was frozen at the beginning of the simulation, which in STAR-CCM+ jargon means that no momentum equations were solved and the velocities were zero for stages 1–3. For both OpenFOAM and DGFlows, non-linear enthalpy-temperature coupling iterations were performed until the desired error tolerance of $tol < 10^{-6}$ was reached. No option was available to avoid solving the momentum equation, however the specified boundary and initial conditions and omission of the Boussinesq source term correctly led to zero velocities throughout the domain.

4.1.3. Results

After the simulated time reached 2500 s, the temperature distribution (Fig. 3) and melting front position (Table 2) were derived. The three codes yielded very similar results. The melting front positions differed by less than 1 mm, which implies that the methods used for calculating one-dimensional heat conduction and resulting phase change are equivalent.

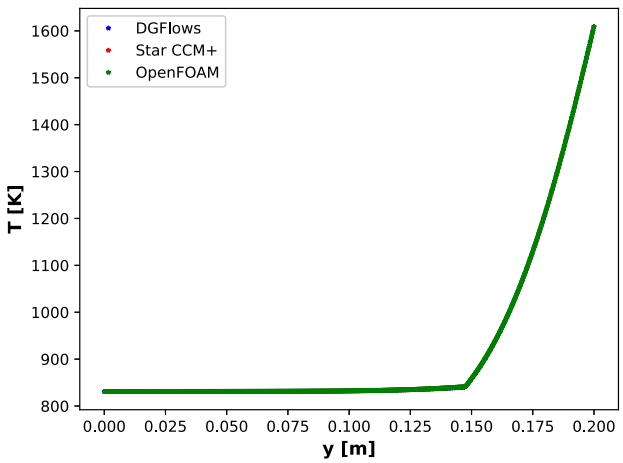

Fig. 3. Temperature vs. y coordinates for the three codes obtained in stage 1 of the benchmark.

Table 2
Final melting front position in stages 1 and 2 of the benchmark (in mm) obtained by the three codes.

Code	DGFlows	STAR-CCM+	OpenFOAM
Stage 1	147.312	147.426	147.048
Stage 2	146.393	146.180	146.000

Table 3
Time sensitivity analysis on the solid–liquid interface position for the three codes obtained in stage 1, with the position given in mm.

Δt (s)	STAR-CCM+	OpenFOAM	DGFlows
2.0	147.415	147.048	147.312
1.0	147.423	147.048	147.312
0.5	147.426	147.048	147.312
0.1	147.428	147.048	147.312

Table 4
Mesh sensitivity analysis on the solid–liquid interface position for the three codes obtained in stage 1, with the position given in mm.

Mesh size	STAR-CCM+	OpenFOAM	DGFlows
50 × 25	147.536	144.271	146.771
100 × 50	147.484	146.109	147.370
200 × 100	147.426	147.048	147.312
400 × 200	147.425	147.031	147.335

4.1.4. Results of the sensitivity analysis

Fig. 4 shows the temperature and Table 3 compares the position of the melting front at the symmetry axis at the end of the simulation for all time step sensitivity analysis cases. In the same fashion, results of the mesh sensitivity analysis are shown in Fig. 5 (temperature) and Table 4 (melting front).

The time step sensitivity analysis suggests that for stage 1, i.e. with no natural circulation, the model is time-step independent for the 200 × 100 mesh. STAR-CCM+ is the only code with very small changes to the melting front position with an increasing time step, whereas the results obtained by OpenFOAM and DGFlows are exactly the same for each time step studied. The mesh refinement sensitivity analysis suggests that the 200 × 100 mesh yields an accurate result while taking a lower amount of computing time than the more refined case. Surprisingly, even the coarsest mesh of 50 × 25 elements produced good results, whereas Stefan problems are known to be sensitive to the resolution of the mesh (Lacroix and Voller, 1990, Hannoun et al., 2003). Possibly, this is because the large temperature differences over the entire domain lead to a relatively small contribution of the latent heat peak to the total energy balance.

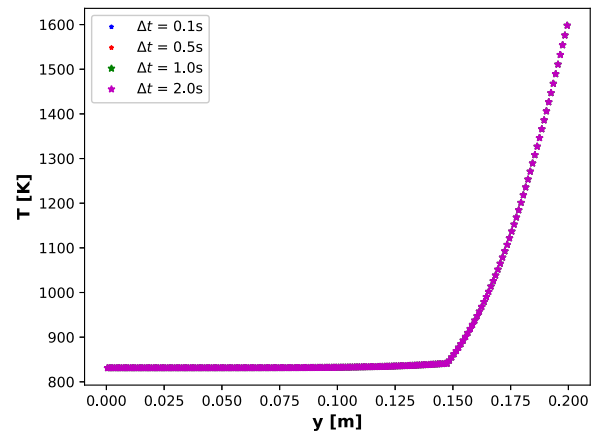

(a) STAR-CCM+

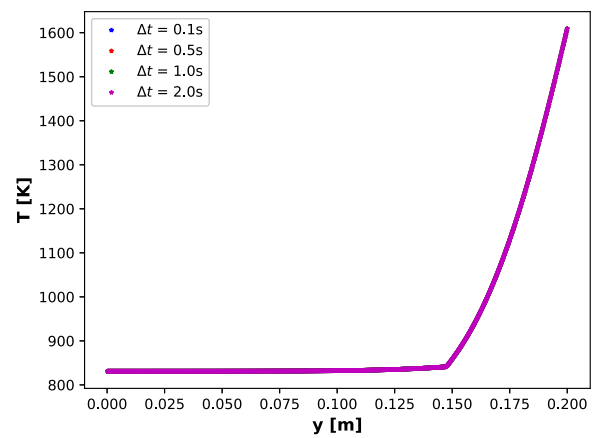

(b) OpenFOAM

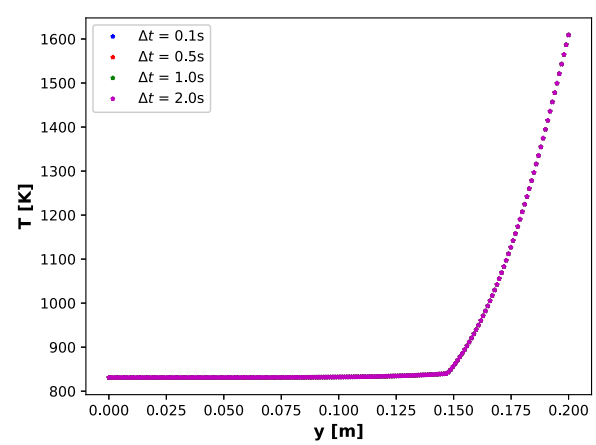

(c) DGFlows

Fig. 4. Temperature vs. y coordinates for the three codes obtained in the time step sensitivity analysis of stage 1.

4.2. Stage 2

4.2.1. Description

In a nuclear reactor, radiation is emitted from within the fuel. Energetic neutrons and photons travel within the reactor vessel and

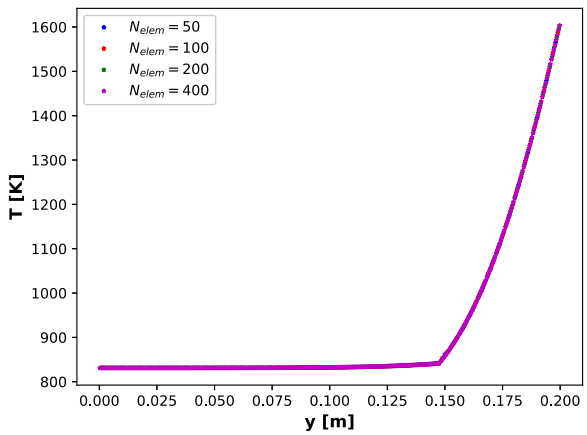

(a) STAR-CCM+

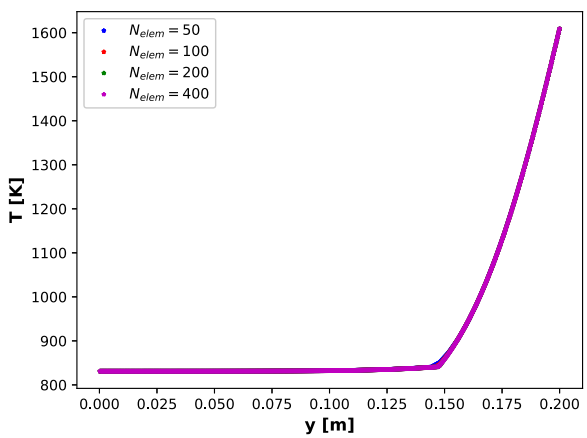

(b) OpenFOAM

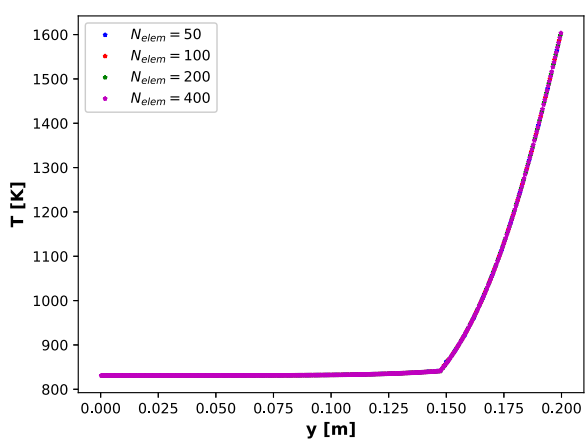

(c) DGFlows

Fig. 5. Temperature vs. y coordinates for the three codes obtained in the mesh refinement sensitivity analysis of stage 1.

heat up the reactor structures. In a molten salt reactor, this heat can also be transferred to the salt that has not undergone fission, such as the solid plug located in the freeze valve. By approximating this heat source to 1% of the decay heat of the reactor, a time-dependent volumetric

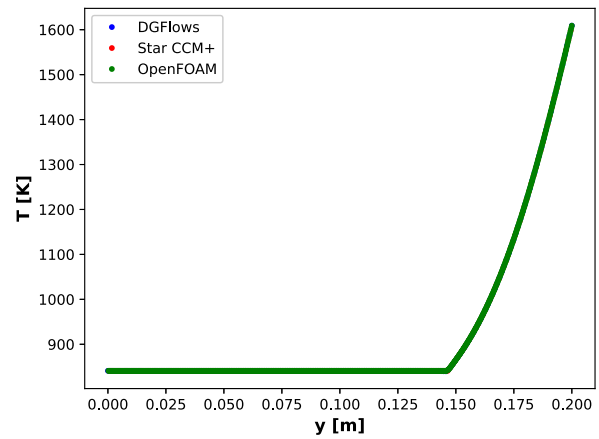

Fig. 6. Temperature vs. y coordinates for the three codes obtained in stage 2 of the benchmark.

Table 5
Thermophysical properties of Hastelloy N used in the benchmark.

Property	Value	Unit
ρ	8860	$\mathrm{kg\,m^{-3}}$
λ	23.6	$\mathrm{W\,m^{-1}\,K^{-1}}$
c_p	578	$\mathrm{J\,kg^{-1}\,K^{-1}}$

heat source H_S is added to the energy equation in the entire salt region of our model (Tano Retamales et al., 2018):

$$H_S(t) = 6.45908 \cdot 10^4 - 6.92 \cdot 10^3 \cdot \ln(t) \qquad (\mathrm{W\,m^{-3}}). \tag{19}$$

4.2.2. Results

After the simulated time of 2500 s, the temperature distribution (Fig. 6) and melting front position (cf. Table 2) were derived. As in stage 1, the three codes yielded similar results. The temperatures are slightly higher than in stage 1 due to the additional heat source, and the melting front shifted by approximately 1 mm towards the bottom.

4.3. Stage 3

4.3.1. Description

As the next step approaching the design of the MSFR freeze valve, a 10 mm thick pipe wall, meshed in the same way as the salt volume, is added to the right side of the model (see Fig. 7). The pipe is made of Hastelloy N with properties taken from Tiberga et al. (2019) and listed in Table 5.

Conjugate heat transfer relations are applied on the interface between the salt and the metallic wall. All other boundaries of the pipe wall are adiabatic, including the top boundary. The initial wall temperature is 831 K. In stage 3, gravity is discarded to analyse how heat conduction from the wall in itself affects the melting process.

Since significant complexity is added to the third benchmark stage, an additional mesh and time step convergence study was performed. The mesh refinements with the 0.5 s time step were: 100 × 55, 200 × 110, 400 × 220, and 800 × 440. Based on the results of the mesh refinement, the 800 × 440 mesh was selected for the final result. Therefore, compared to the mesh-converged solution of stages 1 and 2, the meshing in the third stage is refined by a factor of four. The time steps analysed on the 800 × 440 mesh were 0.5 s and 0.1 s and very little change was observed, suggesting that at these conditions our models are fully converged with respect to the time step.

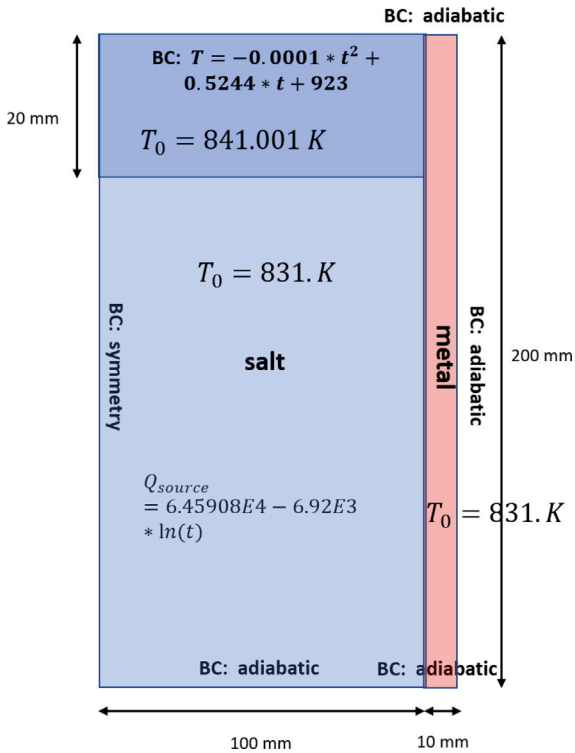

Fig. 7. Geometry with boundary (marked as "BC") and initial conditions (marked as T_0) of stage 3. The dark blue colour indicates the molten salt, the light blue colour indicates the solid salt, and the pink colour represents the metal wall.

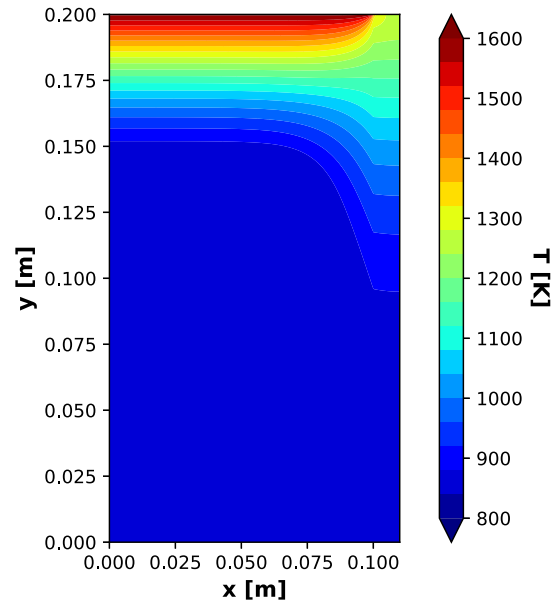

Fig. 8. Temperature contour plot for the entire geometry of stage 3; results taken from OpenFOAM. The 800 × 440 mesh was used with a time step of $\Delta t = 0.5$ s.

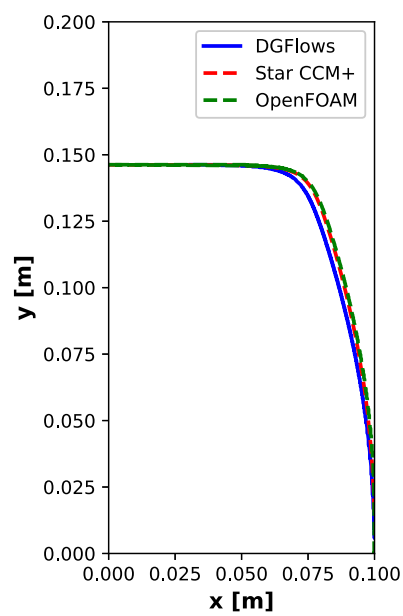

Fig. 9. Melting front positions obtained by the three codes in stage 3. The 800 × 440 mesh was used with a time step of $\Delta t = 0.5$ s.

4.3.2. Implementation

In STAR-CCM+, the wall is a separate solid region with its own properties. A contact interface was created between the wall and the salt and a conjugate heat transfer relation was added (see Section 3.1).

In OpenFOAM, the mesh was decomposed into a solid part (for the Hastelloy) and a liquid part (for both the molten and the frozen salt), each with their own set of thermophysical properties and their own set of initial and boundary conditions. The temperature at the metal-salt interface was calculated based on a harmonic averaging of the heat fluxes (see Section 3.2).

In DGFlows, a material tag was added to the solid and the liquid region, where for each tag a set of thermophysical properties was assigned. At the metal-salt interface, the no-slip condition was imposed, however no explicit treatment was needed for the energy equation as the temperature continuity condition at the interface follows naturally from the penalty terms included in the SIP-DG formulation (see Section 3.3).

4.3.3. Results

Fig. 8 shows the temperature obtained in the third stage with the OpenFOAM model. Whereas the models for stages 1 and 2 yielded quasi one-dimensional results, this was no longer the case for stage 3, since the addition of the metal wall produced a variation of the temperature in the x-direction. Because all boundaries of the metal wall were adiabatic (see Fig. 7), no heat was conducted into the metal wall from the top and therefore the highest temperature values can be found within the salt. Due to the better thermal conductive properties of Hastelloy N compared to the salt, below a height of approximately $y = 0.17$ m, higher temperatures and an enhanced melting rate were observed in the vicinity of the wall. The melting fronts for the mesh-converged solution of 800 × 440 cells obtained by the three codes are plotted in Fig. 9. Whereas a near-perfect agreement between the three codes was observed for the previous two stages, a discrepancy can now be seen between the melt front positions of DGFlows on the one hand, and OpenFOAM and STAR-CCM+ on the other. The discrepancy appears to be larger in the region close to the Hastelloy wall.

To further shed light on this matter, three locations of interest were chosen, for which results are probed along a vertical line, at: $x = 0$ mm, $x = 75$ mm, and $x = 95$ mm. Temperature profiles for all three probes at $t = 2500$ s are plotted in Fig. 10. From the temperature probes, one can observe that far away from the Hastelloy wall, at $x = 0$, the agreement between the three codes is excellent, however as one moves closer to the wall, DGFlows produces different results from the other codes.

The results for benchmark stage 3 show that the conjugate heat transfer between the solid wall and the melting salt appears to introduce a discrepancy in the modelling behaviour of the three codes. A separate validation was performed for the conjugate heat transfer

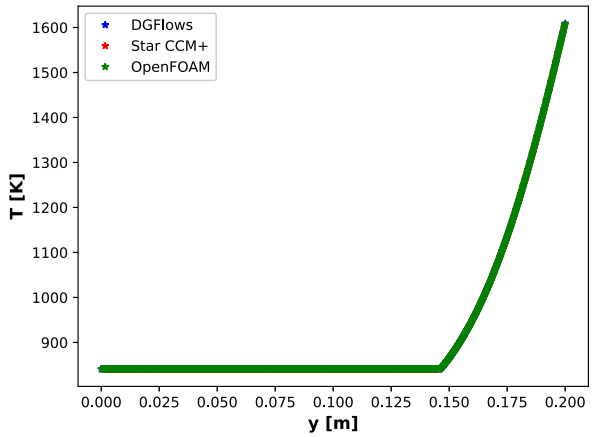

(a) $x = 0$ mm

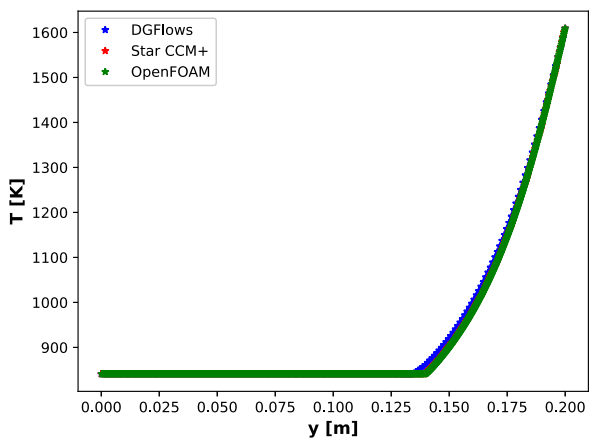

(b) $x = 75$ mm

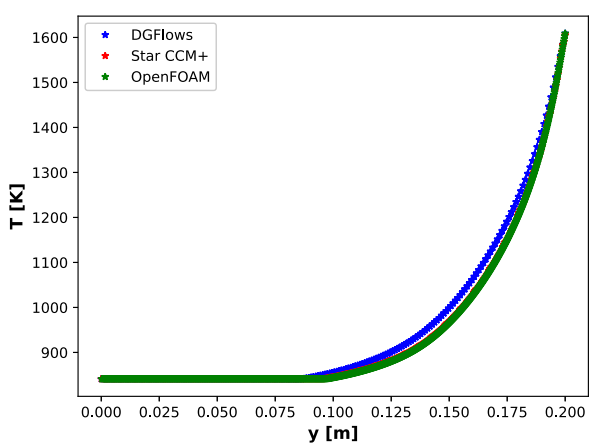

(c) $x = 90$ mm

Fig. 10. Temperature vs. y coordinates for the three codes obtained in stage 3 of the benchmark. Results taken at three different x locations.

without phase change with the use of a different model, where virtually identical results were observed between DGFlows and STAR-CCM+. Based on these observations, we believe the coupling between the conjugate heat transfer and the non-linear phase change phenomena are the source of disagreement between DGFlows on the one hand, and STAR-CCM+ and OpenFOAM on the other.

Note that the three codes adopt different modelling strategies for the conjugate heat transfer. OpenFOAM solves the heat equation in the salt and metal domains sequentially (i.e. first the heat equation in the salt is solved, then the heat equation in the metal), whereas in DGFlows the heat equation is solved for the full domain and no distinction is made between the solid and the liquid regions. In STAR-CCM+, a segregated solver was used, which is a method similar to the one used by OpenFOAM.

It is possible that the simultaneous solution of the heat transport equation leads to a faster melting in the vicinity of the Hastelloy wall with respect to a sequential solution of the heat transport equations, since the salt immediately experiences the presence of the enhanced heat transfer through the metal wall, instead of the solution of the heat transfer through the metal wall lagging behind that of the salt. However, we would expect that the discrepancy between the codes would become smaller for smaller time steps, which does not seem to be the case, see Section 4.3.4. Due to a lack of a suitable analytical or experimental reference solution, we cannot say which of the three codes produces the most correct results. For now, we identify the coupling of the conjugate heat transfer and solid–liquid phase change modelling as a potential source of discrepancy between numerical software and we recommend to take this matter into consideration when modelling the MSFR freeze valve.

4.3.4. Results of the sensitivity analysis

Fig. 11 shows the results of the mesh refinement sensitivity study. With every refinement step, the difference between the results from the previous coarser mesh and the new finer mesh becomes smaller. STAR-CCM+ showed the largest sensitivity to the mesh size, whereas DGFlows' results did not vary significantly between the different mesh refinement cases. Possibly, this is due to the high accuracy of the discontinuous Galerkin method in calculating the discontinuity in the temperature gradient at the interface between the solid and the liquid salt, thus preserving the overall accuracy of the numerical scheme at the metal wall. It was decided that the 800×440 mesh should be used for this and next benchmark stages. Fig. 12 shows the sensitivity of the temperature results to the time step. For all three codes, very little difference could be observed between a time step of $\Delta t = 0.5$ s and $\Delta t = 0.1$ s, and therefore $\Delta t = 0.5$ s was used for the rest of the analysis of stage 3.

4.4. Stage 4

4.4.1. Description

In stage 4, we allow for natural circulation. Salt closest to the heated wall will have a lower density and will start flowing upwards. To model the free convection of the salt, we use the Boussinesq approximation:

$$M_S = -\rho g \beta \cdot (T_{ref} - T) \qquad (\mathrm{N\,m^{-3}}) \tag{20}$$

where the salt's thermal expansion factor is $\beta = 2.5 \cdot 10^{-4}\,\mathrm{K}^{-1}$, based on the density data in Beneš and Konings (2009), the gravitational acceleration $g = 9.81$ m s^{-2}, and the reference temperature $T_{ref} = 831$ K. The dynamic viscosity of the salt is approximated to $\mu = 7.5 \cdot 10^{-3}$ Pa s (Beneš and Konings, 2009) and a fully laminar and incompressible flow is assumed.

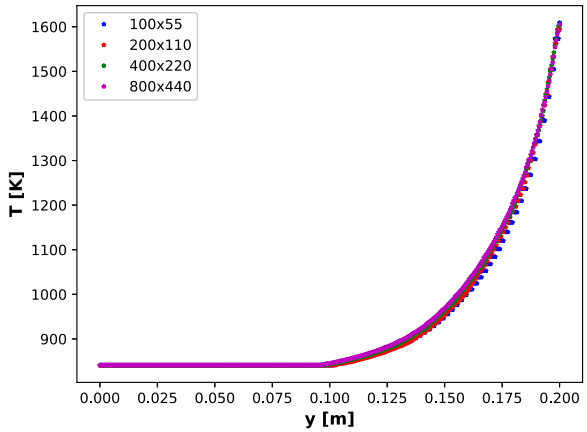

(a) STAR-CCM+

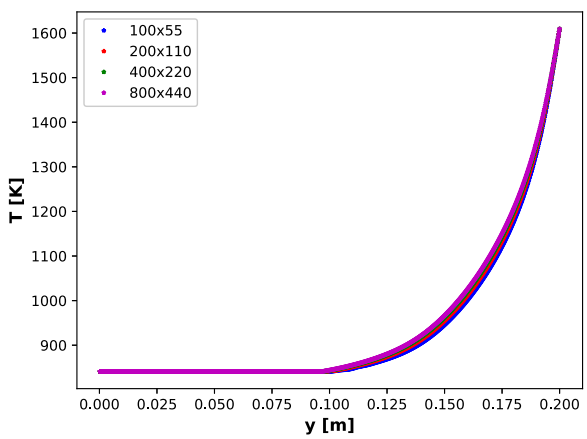

(b) OpenFOAM

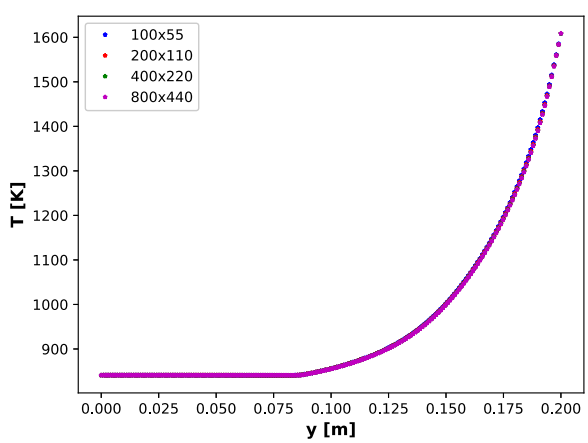

(c) DGFlows

Fig. 11. Temperature vs. y coordinates for the three codes obtained in the mesh refinement sensitivity analysis of stage 3. Results shown for $x = 90$ mm. Here, a time step of $\Delta t = 0.5$ s was used.

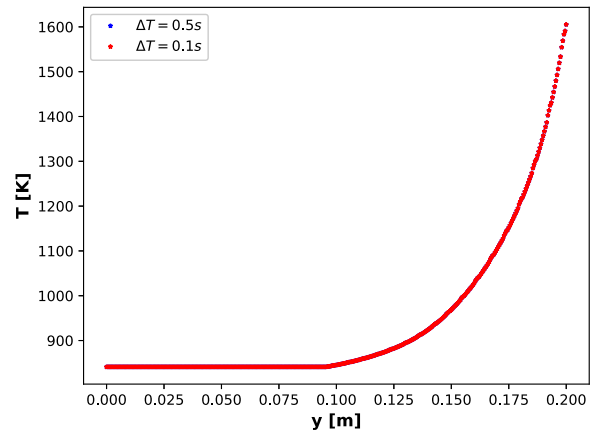

(a) STAR-CCM+

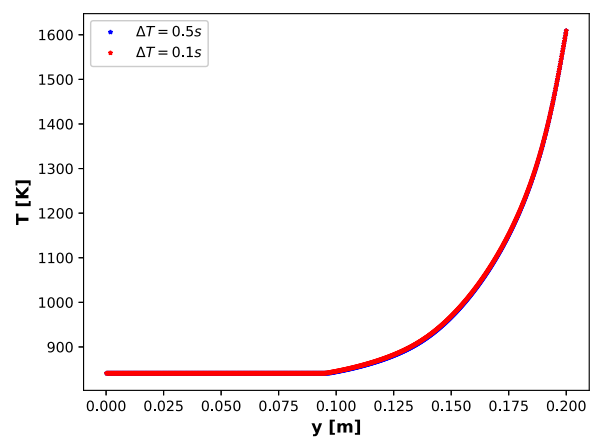

(b) OpenFOAM

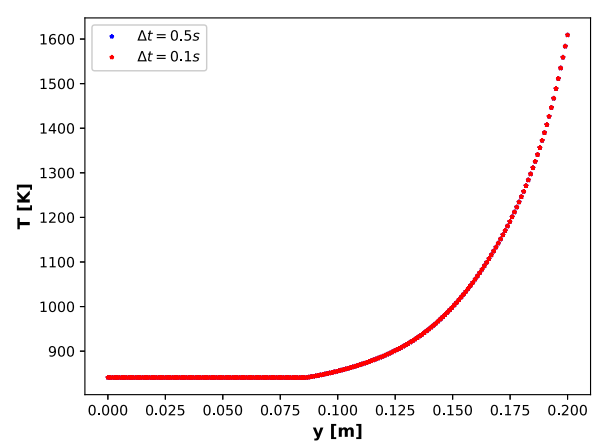

(c) DGFlows

Fig. 12. Temperature vs. y coordinates for the three codes obtained in the time step sensitivity analysis of stage 3. Results shown for $x = 90$ mm. Here, a mesh of 800×440 elements was used.

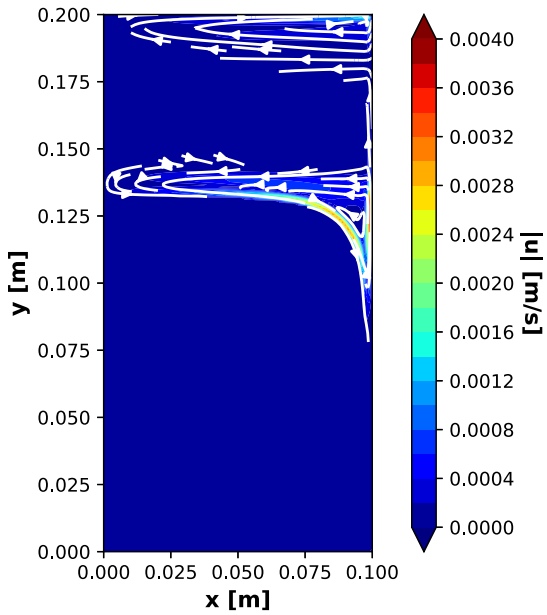

Fig. 13. Contour plot of the flow field with streamlines for stage 4. Results obtained with OpenFOAM, with a 800 × 440 mesh and a time step of $\Delta t = 0.1$ s. A cut-off velocity of $4 \cdot 10^{-5}\,\mathrm{m\,s^{-1}}$ (i.e. approximately 1% of the maximum velocity) was used for the streamlines.

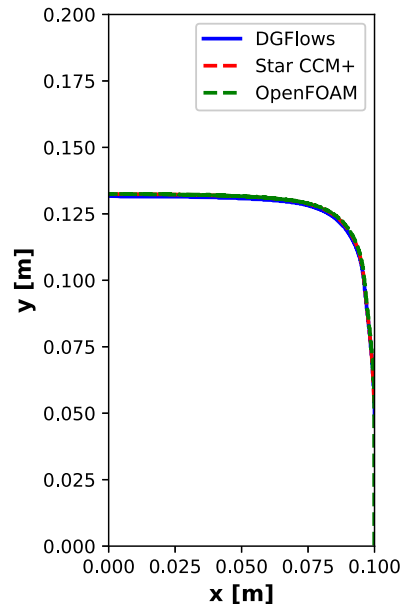

Fig. 14. Melting front positions obtained by the three codes in stage 4. The 800 × 440 mesh was used with a time step of $\Delta t = 0.1$ s.

4.4.2. Implementation

The time step was lowered to 0.1 s for stages 4 and 5 to account for the increased convergence requirements (i.e. Courant number below 1) when changing the model from conduction only to convective phase change. In STAR-CCM+, in stages 4 and 5, the maximum number of inner iterations was changed from 30 to 90 to achieve better convergence. In both OpenFOAM and DGFlows, three outer iterations were added to better resolve the velocity-temperature coupling. Computational requirements increase significantly from stage 3 to stage 4, as a set of new equations is added to the model in addition to reducing the time step and increasing the number of iterations.

4.4.3. Results

Fig. 13 shows the absolute flow velocity for the fourth benchmark stage, also showing the streamlines. A maximum velocity of around $u = 4\ \mathrm{mm\,s^{-1}}$ is reached, corresponding to a Reynolds number of $Re \approx 468$. Therefore, our assumption of laminar flow is justified. Two recirculation zones can be observed, one near the top of the domain where the salt is being heated and one near the melting front. One may observe the salt flow up along the warmer Hastelloy wall and down along the melting front.

Fig. 14 shows a comparison of the melting front positions for all three codes. The addition of natural convection, as opposed to heat conduction dominated phase change, results in an increase of the melting rate and compared to stage 3, more of the salt has melted. However, similarly to what has been observed by Aji (2020), the effect of natural convection slows down the melting of the freeze plug at the sides, thus prolonging its opening time. Instead, the heat transfer is shifted towards the top side of the plug.

In addition, a significantly better agreement was observed between the three codes. We believe this is because the higher heat transfer within the bulk of the salt, induced by the natural convection, reduces the local effect that the solid wall has on the overall melting rate. The better agreement in stage 4, as opposed to stage 3, further supports our hypothesis that the coupling of the heat transfer within the salt and the metal domains was the source of discrepancy between STAR-CCM+, OpenFOAM, and DGFlows.

Fig. 15 depicts the absolute velocity profiles for all three codes, evaluated at the same x-locations selected for stage 3 (i.e. $x = 0$ mm, $x = 75$ mm, and $x = 90$ mm). Fig. 16 shows the temperature profiles at these locations. Similar results are obtained for the absolute velocity profiles for all three codes, although small differences are still visible. Interestingly, for $y = 90$ mm, the velocity results for OpenFOAM appear to deviate from those obtained by STAR-CCM+ and DGFlows; the code predicts a lower peak value of the velocity around $y = 0.12$ m. Regarding the temperature profiles, an excellent agreement between the three codes was obtained, with the results hardly distinguishable from each other.

4.5. Stage 5

4.5.1. Description

In a molten salt reactor, the fuel salt above the top of the freeze valve is not stagnant, but is assumed to be in motion, both during normal operation and emergency drainage of the fuel salt into the dump tanks. The movement of the salt at the freeze valve's top boundary might influence the dynamics of the phase change. In our model, circulation is enforced by moving the top lid in the positive x direction with a tangential velocity of $0.01\ \mathrm{m\,s^{-1}}$. This value was sufficiently high to influence the melting behaviour of the freeze valve, but sufficiently low such that our assumption of laminar flow is still valid.

4.5.2. Results

Fig. 17 shows the absolute velocity and Fig. 18 shows the melting front positions for stage 5. Compared to stage 4, higher velocities are observed in the recirculation zone near the top of the domain, as a consequence of the velocity boundary condition now imposed at the top wall. However, this boundary condition does not seem to significantly impact the flow in the rest of the domain. Whilst the differences between the fourth and the fifth benchmark stage are small, the higher degree of mixing at the top leads to a small increase of the melting rate, as can be seen from the overall position of the melting front. Similarly to stage 4, a very good agreement was observed between the three codes.

Finally, one can now have a look at the development of the melting front from the simpler to the more detailed model, depicted in Fig. 19.

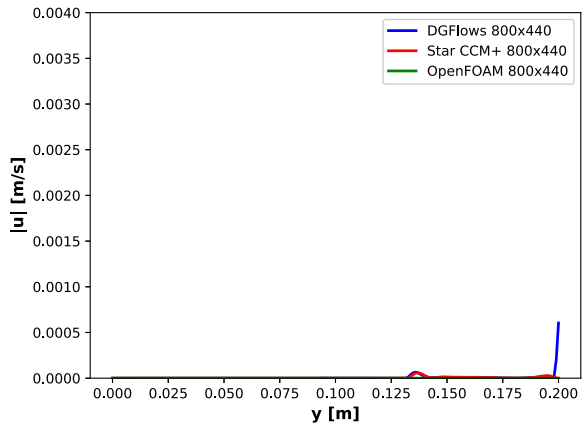

(a) $x = 0$ mm

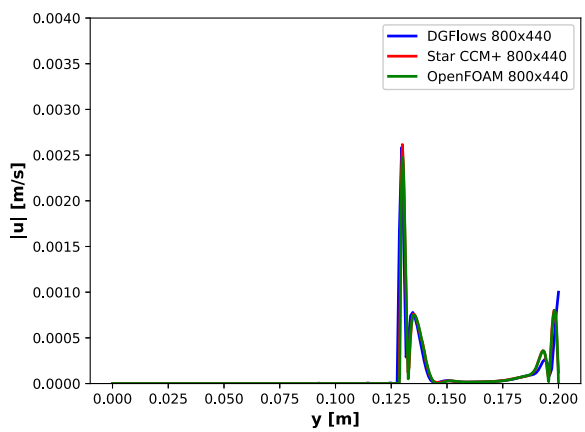

(b) $x = 75$ mm

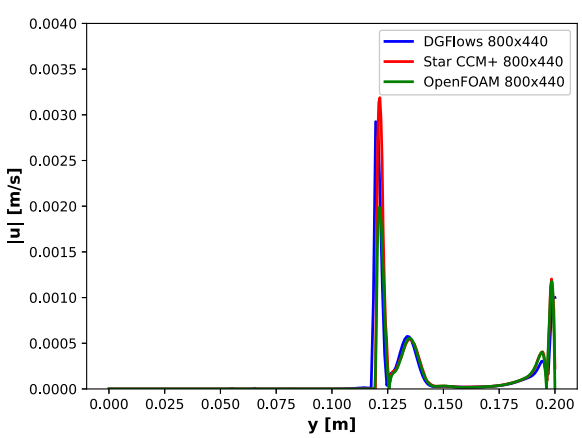

(c) $x = 90$ mm

Fig. 15. Absolute velocity profiles obtained by the three codes in stage 4. Results taken at three different x locations.

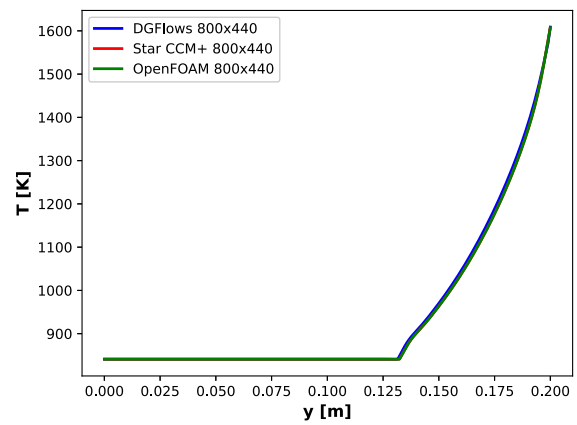

(a) $x = 0$ mm

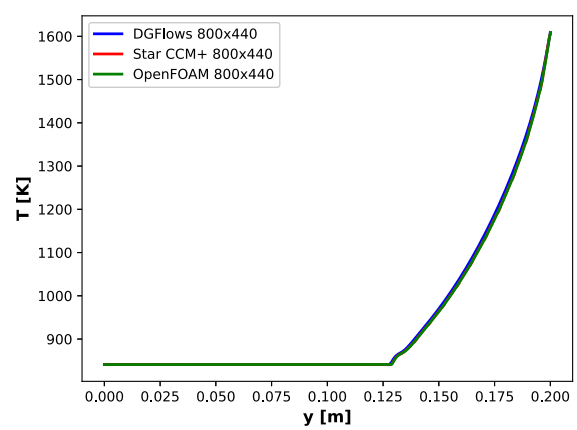

(b) $x = 75$ mm

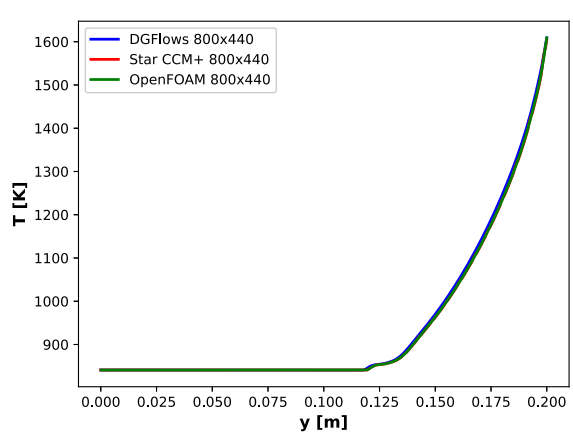

(c) $x = 90$ mm

Fig. 16. Temperature vs. y coordinates for the three codes obtained in stage 4. Results taken at three different x locations.

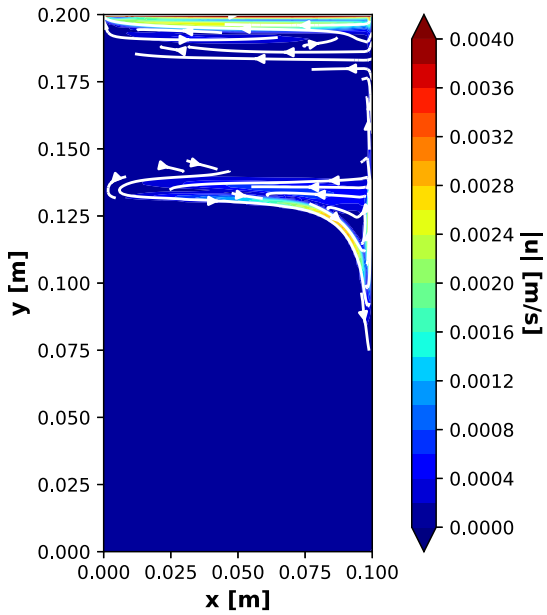

Fig. 17. Contour plot of the flow field with streamlines for stage 5. Results obtained with OpenFOAM, with a 800 × 400 mesh and a time step of $\Delta t = 0.01$ s. A cut-off velocity of $4 \cdot 10^{-5}\,\mathrm{m\,s^{-1}}$ was used for the streamlines.

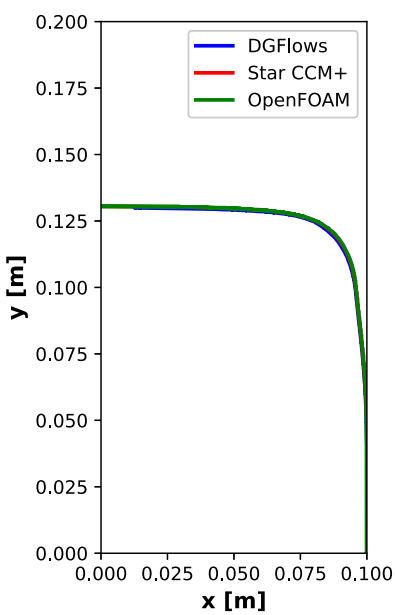

Fig. 18. Melting front positions obtained by the three codes in stage 5. The 800 × 440 mesh was used with a time step of $\Delta t = 0.01$ s.

The changes in the shape of the melting front between stages 2 and 3, and 3 and 4 are substantial and show the importance of conjugate heat transfer and natural convection. An important figure of merit in the MSFR freeze valve design is the opening time, which is one of the factors that determine whether the proposed design meets the safety requirements. Omitting the Hastelloy wall from the simulations would result in a considerable under-prediction of the freeze valve opening time. On the other hand, neglecting the role of natural convection would lead to an over-prediction of the valve opening time.

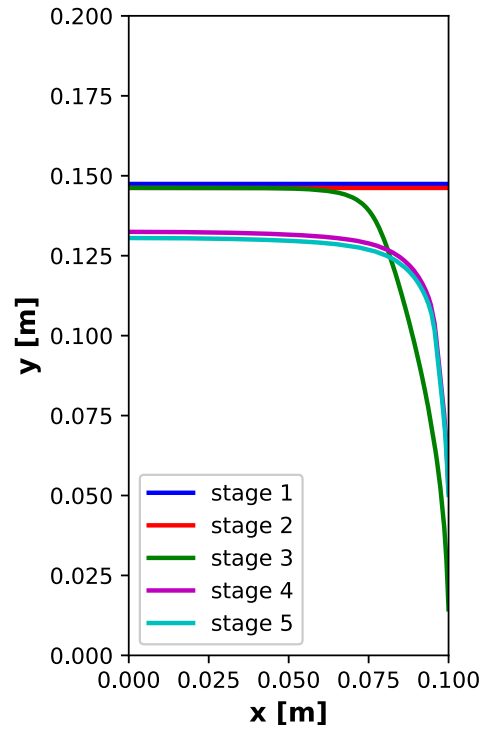

Fig. 19. Melting front positions obtained in all stages of the benchmark by STAR-CCM+.

5. Conclusions

Due to the lack of suitable experimental benchmark data, experimental validation of MSFR freeze valve models is very difficult. In order to help overcome this challenge, this work proposes a numerical benchmark for the MSFR freeze valve consisting of five different stages. A principal feature of this benchmark is a step-wise addition of complexity with every stage of the benchmark. This allows for pinpointing which parts of the model introduce discrepancies between different software suites. Additionally, this benchmark can easily be replicated in other CFD codes. In the present work, results of the benchmark were obtained using solid–liquid phase change models and flow and conjugate heat transfer solvers implemented in STAR-CCM+, OpenFOAM and DGFlows. For all three codes, the melting front position, temperature profiles, and absolute velocity profiles were compared. The results from the benchmark demonstrate a consistent performance of the three codes' phase change models and flow solvers. However, a discrepancy between the results of DGFlows on the one hand, and STAR-CCM+ and OpenFOAM on the other, was observed when adding conjugate heat transfer to the benchmark. This may indicate a different performance of segregated conjugate heat transfer approaches as opposed to fully coupled ones for modelling solid–liquid phase change. For this reason, we recommend carefully considering the conjugate heat transfer modelling approach when simulating the MSFR freeze valve or any other problem where a coupling between conjugate heat transfer and solid–liquid phase change phenomena plays a role. The results from all three codes have been placed in an online repository, and interested users of CFD codes are invited to carry out the benchmark exercise and compare their results and findings with ours, which can help further develop numerical tools dedicated to phase change and molten salt reactors.

CRediT authorship contribution statement

Mateusz Pater: Conceptualization, Methodology, Software, Validation, Analysis & Interpretation of Data, Investigation, Writing – original

draft, Writing – review & editing. **Bouke Kaaks:** Conceptualization, Methodology, Software, Validation, Analysis & Interpretation of Data, Investigation, Writing – original draft, Writing – review & editing. **Bent Lauritzen:** Analysis & Interpretation of Data, Writing – review & editing, Supervision, Funding acquisition. **Danny Lathouwers:** Analysis & Interpretation of Data, Resources(use of inhouse code), Writing – review & editing, Supervision, Funding acquisition.

Declaration of competing interest

The authors declare the following financial interests/personal relationships which may be considered as potential competing interests: Bouke Kaaks reports financial support was provided by European Union. Mateusz Pater reports financial support was provided by European Union. Mateusz Pater reports financial support was provided by Innovation fund Denmark. Mateusz Pater reports a relationship with Seaborg Technologies Aps that includes: employment.

Data availability

Data presented in the figures, to be used for comparison with more codes, can be found under the associated link: https://doi.org/10.5281/zenodo.7821693.

Acknowledgements

This project has received funding from the Euratom research and training programme 2014–2018 under grant agreement no. 847527, as well as through Innovation Fund Denmark's industrial PhD scheme (grant no. 9065-00260).

References

Aji, I.K., 2020. Investigation of basic parameters in developing high-performance freeze valve for molten salt reactor (Ph.D. thesis). University of Electro-Communications.

Balay, S., Gropp, W.D., McInnes, L.C., Smith, B.F., 1997. Efficient management of parallelism in object-oriented numerical software libraries. In: Modern Software Tools for Scientific Computing. Birkhäuser Boston, Boston, MA, pp. 163–202. http://dx.doi.org/10.1007/978-1-4612-1986-6_8.

Belhamadia, Y., Kane, A., Fortin, A., 2012. An enhanced mathematical model for phase change problems with natural convection. Int. J. Numer. Anal. Model. B 2.

Ben-David, O., Levy, A., Mikhailovich, B., Azulay, A., 2013. 3D numerical and experimental study of gallium melting in a rectangular container. Int. J. Heat Mass Transfer 67, 260–271. http://dx.doi.org/10.1016/j.ijheatmasstransfer.2013.07.058.

Beneš, O., Konings, R., 2009. Thermodynamic properties and phase diagrams of fluoride salts for nuclear applications. J. Fluor. Chem. 130 (1), 22–29. http://dx.doi.org/10.1016/j.jfluchem.2008.07.014.

Blanco, J.A., Rubiolo, P., Dumonteil, E., 2020. Neutronic modeling strategies for a liquid fuel transient calculation. In: International Conference on Physics of Reactors: Transition to a Scalable Nuclear Future, PHYSOR 2020. Vol. 2020-March, p. 1016. http://dx.doi.org/10.1051/epjconf/202124706013.

Brent, A.D., Voller, V.R., Reid, K.J., 1988. Enthalpy-porosity technique for modeling convection-diffusion phase change: Application to the melting of a pure metal. Numer. Heat Transfer 13 (3), 297–318. http://dx.doi.org/10.1080/10407788808913615.

Cartland Glover, G., Skillen, A., Litskevich, D., Rolfo, S., Emerson, D.R., Merk, B., Moulinec, C., 2019. On the numerical modelling of frozen walls in a molten salt fast reactor. Nucl. Eng. Des. 355 (March), 110290. http://dx.doi.org/10.1016/j.nucengdes.2019.110290.

Cervi, E., Lorenzi, S., Luzzi, L., Cammi, A., 2019. Multiphysics analysis of the MSFR helium bubbling system: A comparison between neutron diffusion, SP3 neutron transport and Monte Carlo approaches. Ann. Nucl. Energy 132, 227–235. http://dx.doi.org/10.1016/j.anucene.2019.04.029.

Chisholm, B.M., Krahn, S.L., Sowder, A.G., 2020. A unique molten salt reactor feature – The freeze valve system: Design, operating experience, and reliability. Nucl. Eng. Des. 368 (August), 110803. http://dx.doi.org/10.1016/j.nucengdes.2020.110803.

CORDIS, 2014. A paradigm shift in reactor safety with the molten salt fast reactor. URL https://cordis.europa.eu/project/id/661891, (Accessed: 2022-03-31).

CORDIS, 2018. Severe accident modeling and safety assessment for fluid-fuel energy reactors. URL https://cordis.europa.eu/project/id/847527, (Accessed: 2022-03-31).

Dantzig, J.A., 1989. Modelling liquid-solid phase changes with melt convection. Internat. J. Numer. Methods Engrg. 28, 1769–1785.

Faden, M., König-Haagen, A., Brüggemann, D., 2019a. An optimum enthalpy approach for melting and solidification with volume change. Energies 12 (5), http://dx.doi.org/10.3390/en12050868.

Faden, M., König-Haagen, A., Franquet, E., Brüggemann, D., 2021. Influence of density change during melting inside a cavity: Theoretical scaling laws and numerical analysis. Int. J. Heat Mass Transfer 173, http://dx.doi.org/10.1016/j.ijheatmasstransfer.2021.121260.

Faden, M., Linhardt, C., Höhlein, S., König-Haagen, A., Brüggemann, D., 2019b. Velocity field and phase boundary measurements during melting of n-octadecane in a cubical test cell. Int. J. Heat Mass Transfer 135, 104–114. http://dx.doi.org/10.1016/j.ijheatmasstransfer.2019.01.056.

Fiorina, C., Clifford, I., Aufiero, M., Mikityuk, K., 2015. GeN-Foam: A novel OpenFOAM® based multi-physics solver for 2D/3D transient analysis of nuclear reactors. Nucl. Eng. Des. 294, 24–37. http://dx.doi.org/10.1016/j.nucengdes.2015.05.035.

Friedman, A., 1968. The Stefan problem in several space variables. Trans. Amer. Math. Soc. 133, 51–87. http://dx.doi.org/10.1090/S0002-9947-1968-0227625-7.

Gau, C., Viskanta, R., 1986. Melting and solidification of a pure metal on a vertical wall. J. Heat Transfer 108, 174–181.

Geuzaine, C., Remacle, J.-F., 2009. Gmsh: A 3-D finite element mesh generator with built-in pre- and post-processing facilities. Internat. J. Numer. Methods Engrg. 79 (11), 1309–1331. http://dx.doi.org/10.1002/nme.2579, URL https://onlinelibrary.wiley.com/doi/10.1002/nme.2579.

Giraud, J., Ghetta, V., Rubiolo, P., Tano Retamales, M., 2019. Development of a cold plug valve with fluoride salt. In: Progress in the Science and Technology of Nuclear Reactors using Molten Salts. 5, (9), http://dx.doi.org/10.1051/epjn/2019005.

Groth-Jensen, J., Nalbandyan, A., Klinkby, E.B., Lauritzen, B., Sabbagh, P., Pedersen, A.V., 2021. Verification of multiphysics coupling techniques for modeling of molten salt reactors. Ann. Nucl. Energy 164, 108578. http://dx.doi.org/10.1016/j.anucene.2021.108578.

Hannoun, N., Alexiades, V., Mai, T.Z., 2003. Resolving the controversy over tin and gallium melting in a rectangular cavity heated from the side. Numer. Heat Transfer B 44 (3), 253–276. http://dx.doi.org/10.1080/713836378.

Hennink, A., Tiberga, M., Lathouwers, D., 2021. A pressure-based solver for low-Mach number flow using a discontinuous Galerkin method. J. Comput. Phys. 425, 109877. http://dx.doi.org/10.1016/j.jcp.2020.109877.

Hirt, C.W., Nichols, B., 1981. Volume of fluid (VOF) method for the dynamics of free boundaries. J. Comput. Phys. 39, 201–225.

Jones, B.J., Sun, D., Krishnan, S., Garimella, S.V., 2006. Experimental and numerical study of melting in a cylinder. Int. J. Heat Mass Transfer 49 (15–16), 2724–2738. http://dx.doi.org/10.1016/j.ijheatmasstransfer.2006.01.006.

Kaaks, B.J., Reus, J.W.A., Rohde, M., Kloosterman, J.L., Lathouwers, D., 2022. Numerical study of phase-change phenomena : a conservative linearized enthalpy approach. In: Nureth (2019). pp. 1–13. http://dx.doi.org/10.5281/ZENODO.5704671.

Kaaks, B.J., Rohde, M., Kloosterman, J.-l., Lathouwers, D., 2023. An energy-conservative DG-FEM approach for solid–liquid phase change. Numer. Heat Transfer B 1–27. http://dx.doi.org/10.1080/10407790.2023.2211231, URL https://www.tandfonline.com/doi/full/10.1080/10407790.2023.2211231.

Karypis, G., Kumar, V., 1998. A fast and high quality multilevel scheme for partitioning irregular graphs. SIAM J. Sci. Comput. 20 (1), 359–392. http://dx.doi.org/10.1137/S1064827595287997, URL http://epubs.siam.org/doi/10.1137/S1064827595287997.

König-Haagen, A., Franquet, E., Faden, M., Brüggemann, D., 2020. Influence of the convective energy formulation for melting problems with enthalpy methods. Int. J. Therm. Sci. 158 (July), http://dx.doi.org/10.1016/j.ijthermalsci.2020.106477.

König-Haagen, A., Franquet, E., Pernot, E., Brüggemann, D., 2017. A comprehensive benchmark of fixed-grid methods for the modeling of melting. Int. J. Therm. Sci. 118, 69–103. http://dx.doi.org/10.1016/j.ijthermalsci.2017.04.008.

Lacroix, M., Voller, V.R., 1990. Finite difference solutions of solidification phase change problems: Transformed versus fixed grids. Numer. Heat Transfer B 17 (1), 25–41. http://dx.doi.org/10.1080/10407799008961731.

Nedjar, B., 2002. An enthalpy-based finite element method for nonlinear heat problems involving phase change. Comput. Struct. 80 (1), 9–21. http://dx.doi.org/10.1016/S0045-7949(01)00165-1.

Siemens Digital Industries Software, 2020. Simcenter STAR-CCM+ Documentation. Version 2020.2.

Stefan, J., 1889. Ueber einige Probleme der Theorie der Wärmeleitung. Wiener Akad. Math. Naturwiss. Abt. 2A, 98, 473–484.

Swaminathan, C.R., Voller, V.R., 1993. On the enthalpy method. Int. J. Numer. Methods Heat Fluid Flow 3 (3), 233–244. http://dx.doi.org/10.1108/eb017528.

Tano, M., Rubiolo, P., Doche, O., 2017. Progress in modeling solidification in molten salt coolants. Modelling Simul. Mater. Sci. Eng. 25 (7), http://dx.doi.org/10.1088/1361-651X/aa8345.

Tano Retamales, M., Rubiolo, P., Giraud, J., Ghetta, V., 2018. Multiphysics study of the draining transients in the molten salt fast reactor. In: International Congress on Advances in Nuclear Power Plants (ICAPP 2018).

Tiberga, M., Hennink, A., Kloosterman, J.L., Lathouwers, D., 2020a. A high-order Discontinuous Galerkin solver for the incompressible RANS equations coupled to the k-e turbulence model. Comput. & Fluids.

Tiberga, M., Lathouwers, D., Kloosterman, J.L., 2020b. A multi-physics solver for liquid-fueled fast systems based on the discontinuous Galerkin FEM discretization. Prog. Nucl. Energy 127 (May), 103427. http://dx.doi.org/10.1016/j.pnucene.2020.103427.

Tiberga, M., de Oliveira, R.G.G., Cervi, E., Blanco, J.A., Lorenzi, S., Aufiero, M., Lathouwers, D., Rubiolo, P., 2020c. Results from a multi-physics numerical benchmark for codes dedicated to molten salt fast reactors. Ann. Nucl. Energy 142, 107428. http://dx.doi.org/10.1016/j.anucene.2020.107428.

Tiberga, M., Shafer, D., Lathouwers, D., Rohde, M., Kloosterman, J.L., 2019. Preliminary investigation on the melting behavior of a freeze-valve for the molten salt fast reactor. Ann. Nucl. Energy 132, 544–554. http://dx.doi.org/10.1016/j.anucene.2019.06.039.

Voller, V.R., Swaminathan, C.R., 1991. ERAL source-based method for solidification phase change. Numer. Heat Transfer B 19 (2), 175–189. http://dx.doi.org/10.1080/10407799108944962.

Voulgaropoulos, V., Brun, N.L., Charogiannis, A., Markides, C.N., 2020. Transient freezing of water between two parallel plates: A combined experimental and modelling study. Int. J. Heat Mass Transfer 153, 119596. http://dx.doi.org/10.1016/j.ijheatmasstransfer.2020.119596.

Weller, H., Tabor, G., Jasak, H., Fureby, C., 1998. A tensorial approach to computational continuum mechanics using object orientated techniques. Comput. Phys. 12, 620–631. http://dx.doi.org/10.1063/1.168744.

Wilson, D.G., Solomon, A.D., Boggs, P.T. (Eds.), 1978. Moving Boundary Problems. Academic Press.